The Astrophysical Journal, 682:384–399, 2008 July 20

THE MID-INFRARED COLORS OF THE INTERSTELLAR MEDIUM AND EXTENDED SOURCES AT THE GALACTIC CENTER

R. G. Arendt,[1,2] S. R. Stolovy,[3] S. V. Ramírez,[4] K. Sellgren,[5] A. S. Cotera,[6] C. J. Law,[7,8] F. Yusef-Zadeh,[7] H. A. Smith,[9] and D. Y. Gezari[10]

Received 2007 October 4; accepted 2008 April 23

ABSTRACT

A mid-infrared (3.6–8 μm) survey of the Galactic center has been carried out with the IRAC instrument on the *Spitzer Space Telescope*. This survey covers the central $2^\circ \times 1.4^\circ$ ($\sim 280 \times 200$ pc) of the Galaxy. At 3.6 and 4.5 μm the emission is dominated by stellar sources, the fainter ones merging into an unresolved background. At 5.8 and 8 μm the stellar sources are fainter, and large-scale diffuse emission from the ISM of the Galaxy's central molecular zone becomes prominent. The survey reveals that the 8-to-5.8 μm color of the ISM emission is highly uniform across the surveyed region. This uniform color is consistent with a flat extinction law and emission from polycyclic aromatic hydrocarbons (PAHs). Models indicate that this broadband color should not be expected to change if the incident radiation field heating the dust and PAHs is $<10^4$ times that of the solar neighborhood. The few regions with unusually red emission are areas where the PAHs are underabundant and the radiation field is locally strong enough to heat large dust grains to produce significant 8 μm emission. These red regions include compact H II regions, Sgr B1, and wider regions around the Arches and Quintuplet clusters. In these regions the radiation field is $\gtrsim 10^4$ times that of the solar neighborhood. Other regions of very red emission indicate cases where thick dust clouds obscure deeply embedded objects or very early stages of star formation.

Subject headings: dust, extinction — Galaxy: center — infrared: ISM

1. INTRODUCTION

The Galactic center (GC) is naturally a region of great interest. The gravitational center of the Galaxy is marked by the supermassive black hole at the radio source Sgr A*. Remarkably, two young, dense stellar disks have been discovered within 0.5 pc orbiting Sgr A* (Paumard et al. 2006). Further out is a molecular ring, or the "circumnuclear disk," enclosing an ionized minispiral structure (e.g., Christopher et al. 2005). These features are within a radius of $\sim$7 pc. A concentration of molecular material is observed out to a radius of $\sim$200 pc along the Galactic plane; this region is known as the central molecular zone (CMZ). Aside from the stellar bulge of the Galaxy, the CMZ encompasses nearly all of the Galactic structures and objects that are characteristic of, or unique to, the GC.

The CMZ is estimated to contain about 10% of the Galaxy's molecular gas content (e.g., Morris & Serabyn 1996; Mezger 1978), or about $(5–10) \times 10^7\ M_\odot$ (e.g., Armstrong & Barrett 1985; Stark et al. 1989). It has a two-component structure. The inner region consists of a set of low-velocity clouds lying on or close to the Galactic plane, including the giant Sagittarius molecular clouds, which together comprise the "disk population" (Morris & Serabyn 1996). The outer set of clouds forms a comparatively high-velocity (130–200 km s^{-1}) quasi-continuous ring structure that surrounds the first one at a radius of $\sim$180 pc (the so-called 180 pc molecular ring; Morris & Serabyn 1996). Analysis of NH_3 and H_3^+ absorption lines in the CMZ has indicated that the molecular gas contains a widespread, relatively hot component ($T \gtrsim 175$ K; Wilson et al. 1982; Oka et al. 2005), which is not found apart from dense molecular cores elsewhere in the Galaxy. Analysis by Hüttemeister et al. (1993) indicates that the molecular gas has at least two phases: a hot phase ($T \sim 200$ K, $n_{H_2} \lesssim 10^3$ cm^{-3}) with a filling factor of $\sim$25% and a cooler component ($T \sim 25$ K, $n_{H_2} \gtrsim 10^4$ cm^{-3}) which fills the remaining 75% of the volume of the molecular clouds.

The average dust temperature in the CMZ appears to be much lower than that of the gas, $T_{dust} \sim 25–30$ K (Odenwald & Fazio 1984; Cox & Laureijs 1989). The much higher gas temperatures therefore indicate the presence of some efficient gas heating mechanisms, and supersonic winds and turbulence had been suspected; the large gas line widths, 15–50 km s^{-1}, are consistent with such ideas, although the details of the mechanisms are debated (supernova remnants [SNRs], outflows, viscous heating effects, etc.). Observation of widespread SiO emission indicates the recent or current presence of strong shocks in the CMZ (Martín-Pintado et al. 1997; Hüttemeister et al. 1998). The discrepancy between dust and gas temperatures has recently been accounted for in terms of the impact of cosmic-ray electrons heating molecular clouds directly and raising their temperatures (Yusef-Zadeh et al. 2007a).

In addition to the molecular gas, the CMZ is also infused with neutral and ionized components, as revealed by enhanced infrared continuum and line emission (e.g., Rodríguez-Fernández et al. 2004; Rodríguez-Fernández & Martín-Pintado 2005) and by enhanced radio continuum emission (e.g., Altenhoff et al. 1979).

[1] CRESST/UMBC, NASA Goddard Space Flight Center, Code 665, 8800 Greenbelt Road, Greenbelt, MD 20771; richard.g.arendt@nasa.gov.
[2] Science Systems and Applications, Inc.
[3] *Spitzer* Science Center, California Institute of Technology, Mail Code 314-6, 1200 East California Boulevard, Pasadena, CA 91125.
[4] Infrared Processing and Analysis Center, California Institute of Technology, Mail Code 100-22, 1200 East California Boulevard, Pasadena, CA 91125.
[5] Department of Astronomy, Ohio State University, 140 West 18th Avenue, Columbus, OH 43210.
[6] SETI Institute, 515 North Whisman Road, Mountain View, CA 94043.
[7] Department of Physics and Astronomy, Northwestern University, Evanston, IL 60208.
[8] Astronomical Institute "Anton Pannekoek," University of Amsterdam, 1098 SJ Amsterdam, Netherlands.
[9] Harvard-Smithsonian Center for Astrophysics, 60 Garden Street, Cambridge, MA 02138.
[10] NASA Goddard Space Flight Center, Code 667, 8800 Greenbelt Road, Greenbelt, MD 20771.

The launch of the *Spitzer Space Telescope* (Werner et al. 2004) provides a new opportunity to investigate the GC at mid- to far-infrared wavelengths with unprecedented sensitivity and spatial resolution. *Spitzer*'s Infrared Array Camera (IRAC; Fazio et al. 2004) provides 5′ field-of-view imaging capabilities with $<2''$ spatial resolution at four broadband mid-infrared channels nominally at 3.6, 4.5, 5.8, and 8 μm. We used IRAC to carry out a $2^\circ \times 1.4^\circ$ ($\sim 280 \times 200$ pc) survey of the GC region, which includes the entire CMZ. An initial summary of the results of this survey has been presented by Stolovy et al. (2006). A more extensive overview will be provided by S. Stolovy et al. (2008, in preparation). The measurement, cataloging, and characterization of point sources observed in our IRAC GC survey are described by Ramírez et al. (2008). In IRAC's 3.6 and 4.5 μm channels, the GC is dominated by stellar emission, both for resolved sources and in the unresolved background. At 5.8 and 8 μm wavelengths, most point sources become significantly fainter, and a strong, structured background produced by the diffuse ISM is dominant. In this study we focus on the diffuse ISM as revealed by IRAC. In particular we investigate what the broadband colors indicate about the nature of the dust producing the emission and the environment in which that dust is found.

Section 2 of this paper contains a brief summary of the IRAC observations. Section 3 presents the colors observed for the diffuse emission and for a few, more compact sources of special interest. Mostly, this focuses on the 5.8–8 μm color of the ISM emission. The shorter wavelength colors are dominated by starlight and extinction (reddening) effects. Section 4 discusses the implications of the uniformity of the color on large scales and the few exceptional regions on small scales. Although limited to the single 5.8–8 μm color, our analysis yields several general robust conclusions concerning the relative abundance of polycyclic aromatic hydrocarbons (PAHs), the strength of the interstellar radiation field (ISRF), and the shape of the extinction law in the GC. The last section (§ 5) contains a summary of this paper.

2. OBSERVATIONS

We observed the central region of the Galaxy using 12 astronomical observation requests (AORs) which mapped the region in $\sim 0.25^\circ$ wide strips at roughly constant declination (a restriction due to *Spitzer*'s pointing constraints and the low ecliptic latitude of the field). Most strips were $\sim 1.75^\circ$ long, except that the one containing Sgr A was split into two parts (to mitigate the potential effects of latent images, with the brightest regions of the survey scheduled last). In addition, those strips at the highest and lowest declinations were shorter, in order to limit the area of complete coverage to $|l| < 1.0^\circ$ and $|b| < 0.7^\circ$. The total area covered in all four channels was ~ 3.5 deg^2, including the additional irregular edges of the region. The medium-scale five-point Gaussian dither pattern was used. This pattern makes small offsets to the telescope pointing, with an average offset of $\sim 30''$. We did not use the smaller scale pattern because it would have provided insufficient dithering for mitigating the stray light artifacts of bright stars and hampered self-calibration of the data (see the Appendix). Frame times of 2 s were used throughout the survey. No regions of extended emission were saturated except at Sgr A at 8 μm, but more than 10^4 bright point sources were saturated in at least one channel (Ramírez et al. 2008). Most saturated sources are isolated point sources, but high densities of saturated sources are found within the bright cluster at Sgr A and the Quintuplet cluster. These areas, and a sample of 12 other saturated sources, were reobserved in subarray mode with 0.02 s frame times to obtain unsaturated data. All analysis in this work was performed on mosaicked images that incorporated the subarray data for these sources.

We constructed our own mosaics from the total set of basic calibrated data (BCD; the standard *Spitzer* data products intended for detailed scientific analysis) from all AORs. The primary description of our processing is given by Stolovy et al. (2006) and S. Stolovy et al. (2008, in preparation). In the Appendix, we provide additional detail concerning aspects of the processing that are particularly relevant in studying the brightness and color of extended emission.

3. ANALYSIS

3.1. *The Diffuse ISM*

3.1.1. *The Large-Scale Distribution of* 8 μm *Intensity and* 8/5.8 μm *Color*

The 8 μm mosaic of the GC region is shown in Figure 1. The general structure of the ISM emission in this region appears similar to that of other regions in the Galactic plane as revealed by the GLIMPSE survey (Benjamin et al. 2003). Both in the GC and in other regions, much of the ISM emission is resolved into elongated arcs and filamentary structures (S. Stolovy et al. 2008, in preparation). Embedded among these are very bright compact regions that contain specific local heating sources. Superimposed infrared dark clouds (IRDCs) have structure similar to that of the emission but are not well correlated with the emission. The ISM emission has a strong unresolved background component, which is often suppressed in depictions meant to highlight the structure of the emission (such as Fig. 1). The most fundamental difference between emission in the GC and that in other regions of the Galactic plane is that the GC emission is several times brighter. Figure 2 shows a wider view of the GC region as seen by SPIRIT III on the *MSX* mission (Price et al. 2001), revealing that the emission within our survey region is brighter than that typically found in the inner galaxy (at $|l| > 1.5^\circ$). Figure 3 provides a more quantitative illustration of the relative brightness of our survey region. The intensity enhancement is loosely correlated with the large-scale distribution of molecular emission in the GC region (e.g., Martin et al. 2004). This indicates that much of the low-latitude ($|b| < 0.2^\circ$) structure in the GC mosaic really is in the central ~ 150 pc radius of the Galaxy, but that the emission does not directly arise from the molecular component of the CMZ.

In contrast, emission at higher latitudes ($|b| > 0.2^\circ$) often appears to be more local features superimposed along the line of sight. One indication of this is association with Hα emission, which would be too heavily extincted to be visible at the distance to the GC, with the possible exception of objects seen at the extreme latitude limits of our survey (Stolovy et al. 2006; S. Stolovy et al. 2008, in preparation). Another is the association with very dark clouds, which must lie relatively close to the Sun. Otherwise, the general foreground emission along the line of sight would reduce the contrast of these features. The large angular scale and presence of fine detail in the higher latitude features also suggest they are relatively nearby clouds along the line of sight. Pauls & Mezger (1975) use the velocity and line widths of 6 cm radio recombination lines to distinguish emission from the GC (large velocities and/or broad lines) from more local emission along the line of sight (velocities near zero and narrow line widths). All of the regions they examined at $|b| > 0.16^\circ$ are characterized as being along the line of sight, rather than at the GC.

Figure 4 shows the ratio of 8 μm/5.8 μm emission, i.e., the $I(8\ \mu\text{m})/I(5.8\ \mu\text{m})$ color. In this ratio virtually all of the diffuse emission features disappear, indicating that they have a very

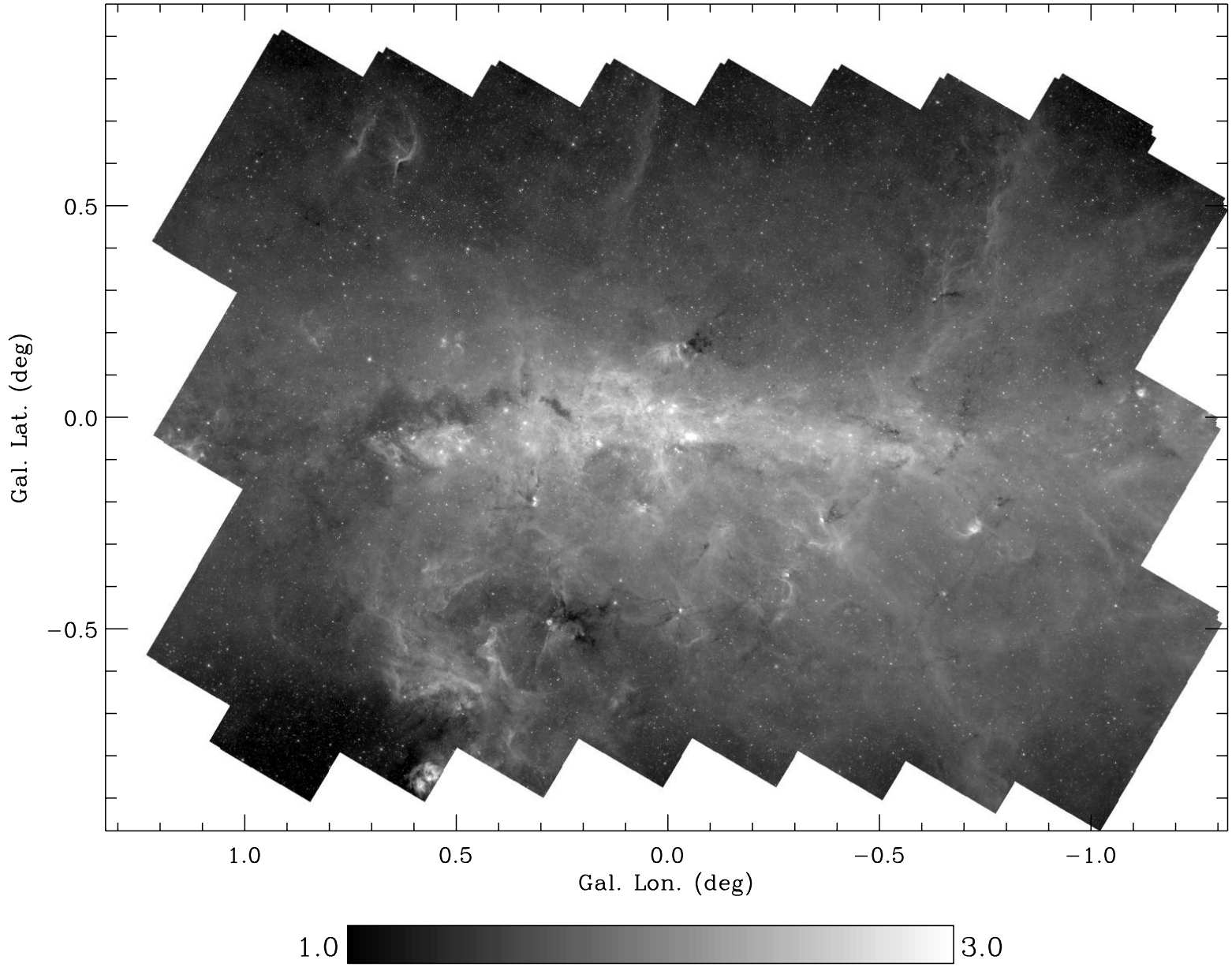

FIG. 1.—Mosaic of the *Spitzer* IRAC GC survey at 8 μm. Intensities are scaled logarithmically from 10 to 10^3 MJy sr^{-1}. The brightest diffuse emission is correlated with the CMZ.

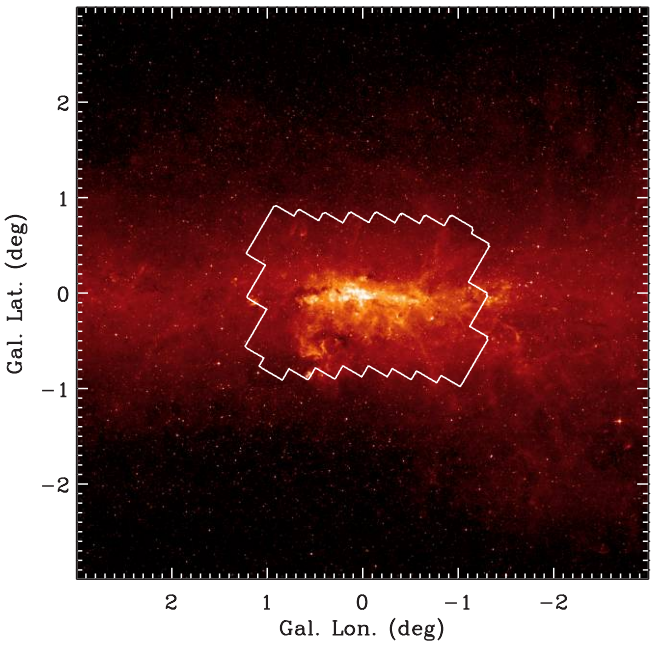

FIG. 2.—GC region at 8.28 μm as seen by the *MSX* mission (logarithmic intensity scale). The white contour indicates the extent of our *Spitzer* IRAC survey. The bright CMZ at a galactocentric radius of $r < 100$ pc is clearly distinct from the wider span of the inner galaxy, $3^\circ > l > -3^\circ$ ($r < 400$ pc).

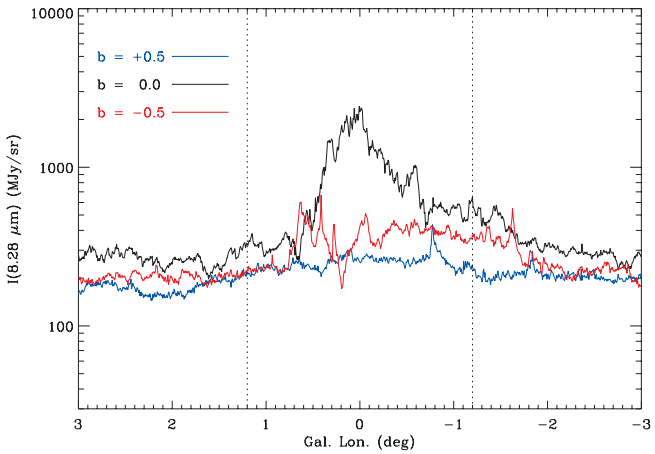

FIG. 3.—Intensity slices through the *MSX* 8.28 μm data at several latitudes. The data have been binned to 24″ pixels, and medians are taken over a 6.8′ swath in latitude. The slice at $b = 0$ shows that the structures of the CMZ are 2–10 times brighter than the emission in other parts of the Galactic plane.

uniform color that is independent of brightness. Dark regions in the ratio map indicate bluer colors associated with numerous individually resolved stars and with the unresolved stellar background, which becomes comparatively bright in the innermost regions of the galaxy (central $\sim 10'$). There are only a few unusually red point sources. Two of these are asteroids (1567 Alikoski and 459 Signe), and two others are PN M1-26 (HD 316248; Sahai & Trauger 1998) and the candidate PN 359.491+0.316 (IRAS 17399−2910; Becker et al. 1994). Brighter (i.e., redder) extended regions in the ratio map are associated with a few special types of emission features, which are discussed below, and with the darkest of the IRDCs [e.g., the complex near $(l, b) = (0.24^\circ, -0.45^\circ)$]. The apparent redness of the IRDCs may be an artifact of residual errors in the subtraction of the zodiacal light or instrumental offsets (see the Appendix and Table 1). Small offset errors would have the greatest impact on the faintest regions of the images, which are the IRDCs and regions at extreme latitudes along the edges of the mosaics.

3.1.2. *ISM Colors Corrected for the Effect of Unresolved Starlight*

To better isolate the ISM emission, we have subtracted stellar emission in a manner similar to that applied to external galaxies (Pahre et al. 2004). In effect, we decompose the 8 and 5.8 μm emission into ISM and stellar components using the 4.5 μm emission as a strong tracer of the starlight. We assume that there exist fixed spatial templates of each component, such that

$$I(\lambda) = \alpha_\lambda I_{\rm ISM} + \beta_\lambda I_{\rm stellar}, \qquad (1)$$

where $I(\lambda)$ is the observed emission at $\lambda = 4.5$, 5.8, or 8 μm; $I_{\rm ISM}$ and $I_{\rm stellar}$ are fixed (but unknown) templates of the ISM and stellar emission; and α_λ and β_λ are the scaling factors for the respective templates. The ratios of the α_λ- or β_λ-coefficients yield the colors of the ISM and stellar emission at the relevant wavelengths. If the ISM emission were negligible at 4.5 μm and stellar emission were negligible at 8 μm, then $\alpha_{4.5\ \mu{\rm m}} = \beta_{8\ \mu{\rm m}} = 0$, and a linear least-squares fit of the form

$$I(5.8\ \mu{\rm m}) = A[I(8\ \mu{\rm m})] + B[I(4.5\ \mu{\rm m})] + C \qquad (2)$$

could be used to determine $A = \alpha_{5.8\ \mu{\rm m}}/\alpha_{8\ \mu{\rm m}}$, the mean 5.8/8 μm color of the ISM; $B = \beta_{5.8\ \mu{\rm m}}/\beta_{4.5\ \mu{\rm m}}$, the mean 5.8/4.5 μm color of the starlight; and C, a constant term representing a linear combination of the mean systematic errors (including those of the detector offsets, zodiacal light, and the stellar model) in all three channels. However, because there is no a priori knowledge of the magnitude or sign of the systematic errors in each channel, we attribute this term to only the 5.8 μm channel, which exhibits the greatest instability in detector offset.

In reality, the longer wavelength stellar emission and shorter wavelength ISM emission are not negligible. Therefore, the interpretation of the A-, B-, and C-coefficients derived in equation (2) is slightly more complicated. To derive both $\beta_{5.8\ \mu{\rm m}}/\beta_{4.5\ \mu{\rm m}}$ and $\beta_{8\ \mu{\rm m}}/\beta_{4.5\ \mu{\rm m}}$ from A and B, we must assume the color of the starlight at one pair of wavelengths. We choose to set the same $[5.8] - [8.0] = +0.04$ mag theoretical color that was adopted by Pahre et al. (2004), as these colors should be least affected by extinction. Then we can appropriately scale and subtract $I(4.5\ \mu{\rm m})$ from the 5.8 and 8 μm emission to remove the mean stellar emission at each of these wavelengths. The derived $[4.5] - [5.8]$ and $[4.5] - [8.0]$ colors are about 0.1 mag redder than those used by Pahre et al. (2004). Because $I(4.5\ \mu{\rm m})$ also contains a weak $I_{\rm ISM}$ component, after this subtraction of the starlight the ISM emission is slightly underestimated. The factor by which the ISM is reduced can be calculated from A and B, if we again assume the color of the ISM emission at one set of wavelengths. We use the "BARE-GR-FG" interstellar dust model of Zubko et al. (2004) to calculate that $\alpha_{4.5\ \mu{\rm m}}/\alpha_{5.8\ \mu{\rm m}} = 0.194$. From this we find that using $I(4.5\ \mu{\rm m})$ as a template of the starlight leads to underestimating the ISM emission by factors of 0.85 and 0.97 at 5.8 and 8 μm, respectively. To summarize, we construct

$$I_{\rm ISM}(8\ \mu{\rm m}) = [I(8\ \mu{\rm m}) - 0.449 I(4.5\ \mu{\rm m})]/0.97 \qquad (3)$$

and

$$I_{\rm ISM}(5.8\ \mu{\rm m}) = [I(5.8\ \mu{\rm m}) - 0.777 I(4.5\ \mu{\rm m})]/0.85 + 1.68. \qquad (4)$$

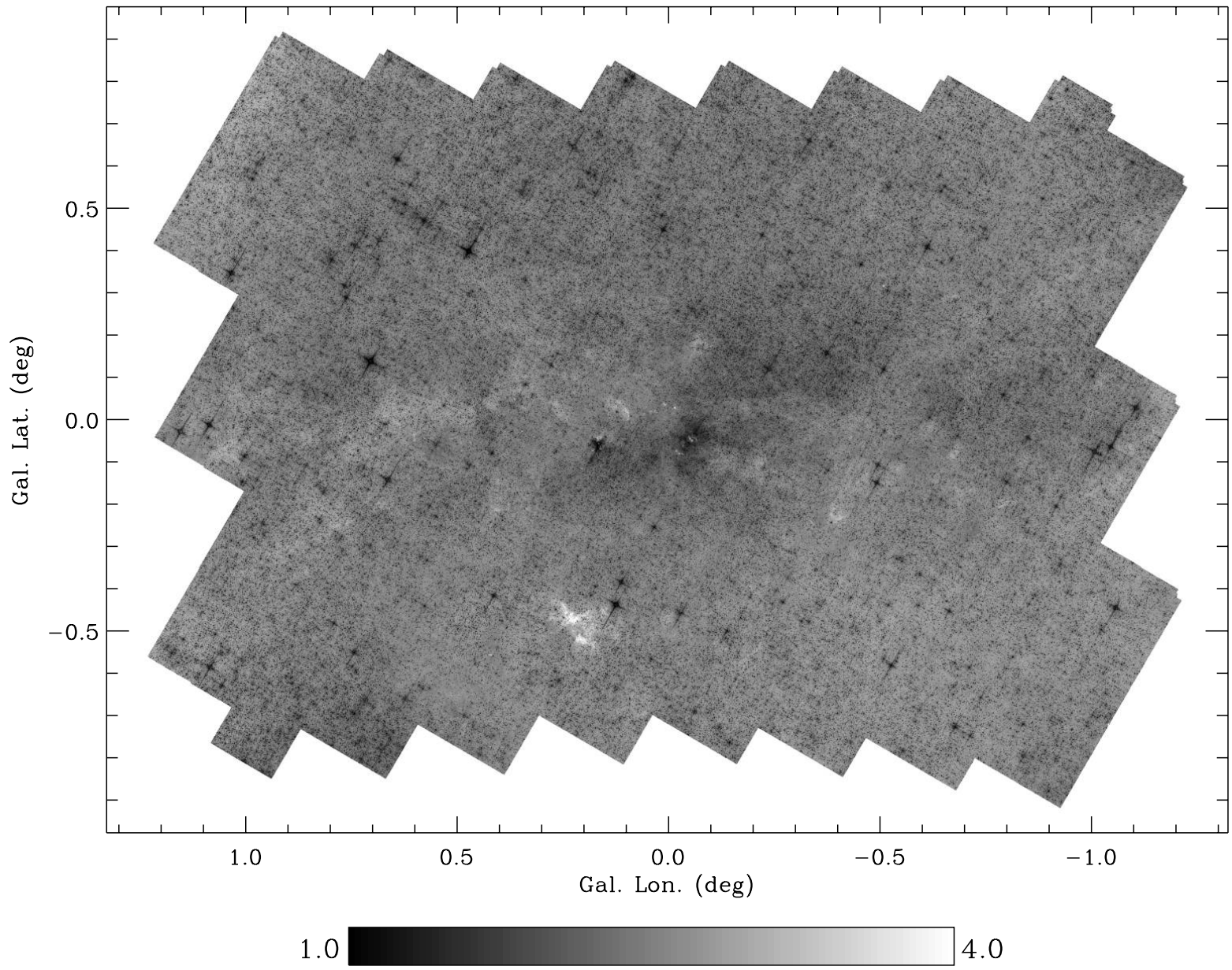

FIG. 4.—GC region depicted in $I(8\ \mu\text{m})/I(5.8\ \mu\text{m})$ color (*linear gray scale*). This color shows little variation or correlation with the 8 μm intensity (Fig. 1). Stellar sources have $I(8\ \mu\text{m})/I(5.8\ \mu\text{m}) < 1$ and appear black here. Only a few extended regions have redder than average colors. Several of these are shown in detail in Figs. 6 and 7. The distinct complex near $(l, b) = (0.24^\circ, -0.45^\circ)$ is at the darkest of the IRDCs, and thus may be affected by small errors in subtraction of the zodiacal light emission or detector offsets.

TABLE 1
Comparison of the Observed Sky Intensities and Offset Terms

Wavelength (μm)	I (MJy sr^{-1})		Mean Z (MJy sr^{-1})	F^p (MJy sr^{-1})		F^q (MJy sr^{-1})		
	Median	Mean		Median	Mean	σ	Median	Max.
3.6	14.1	23.9	0.097	−0.0367	0.0173	0.186	0.0139	1.92
4.5	11.0	18.5	0.193	−0.0613	0.0110	0.201	0.00906	0.874
5.8	26.7	33.9	1.298	0.0331	0.0686	0.930	0.0839	8.49
8	66.1	77.1	6.181	−0.0663	−0.315	9.14	0.659	99.3

Notes.—Here I is the observed intensity in the final image, Z is the difference between the zodiacal light toward the GC and that toward the sky-dark calibration field, F^p is the self-calibration detector offset per detector pixel p, and F^q is the self-calibration detector offset per frame q.

The 8/5.8 μm ISM colors found after subtraction of the starlight (and offset error) are slightly redder and no longer differ at regions of high extinction, but they otherwise appear quite uniform over a wide range of brightness. This is depicted in Figure 5, where the color is plotted as a function of the 8 μm brightness. The colors shown here are those of the integrated emission along the line of sight. The shading of this figure is scaled to the log of the number of pixels with a given color-brightness combination. This logarithmic scaling enhances the visibility of the outliers in the color. Some of the unusually red extended regions that stand out in the $I(8\ \mu\mathrm{m})/I(5.8\ \mu\mathrm{m})$ colors (both before and after subtraction of starlight) are highlighted and are discussed in § 3.2. The median color ($\pm 1\ \sigma$ standard deviation) is $I_{\mathrm{ISM}}(8\ \mu\mathrm{m})/I_{\mathrm{ISM}}(5.8\ \mu\mathrm{m}) = 2.71 \pm 0.19$, independent of the 8 μm brightness. The locations of bright stellar sources have been excluded from this plot with an intensity threshold cut at 70 MJy sr^{-1} at 4.5 μm and by excluding regions with $I(8\ \mu\mathrm{m})/I(5.8\ \mu\mathrm{m}) < 2.3$ (before the subtraction of starlight), but remaining faint resolved stars and systematic errors in using the 4.5 μm emission as the template cause much of the dispersion toward redder colors at low intensities (<50 MJy sr^{-1}). The observed $I_{\mathrm{ISM}}(8\ \mu\mathrm{m})/I_{\mathrm{ISM}}(5.8\ \mu\mathrm{m})$ colors in the GC are similar to (although slightly bluer than) the colors observed by Flagey et al. (2006) in six regions at longitudes $l = 27.5^\circ$, 105.6°, and 254.4°. (These latter colors are indicated by the arrows in Fig. 5.) The difference is established using a two-tailed Kolmogorov-Smirnov test, which yields a maximum deviation between the cumulative distribution function of $D = 0.58$. For the given number of data points, if the two distributions are intrinsically the same, the probability of D exceeding this value is 0.02. Therefore, this test finds only a 2% chance that the Flagey et al. (2006) results are consistent with a random sampling of the colors that we measure near the GC. However, while this statistic indicates that the colors are likely to be different, we cannot rule out that procedural differences or systematic errors are the cause of the apparent differences.

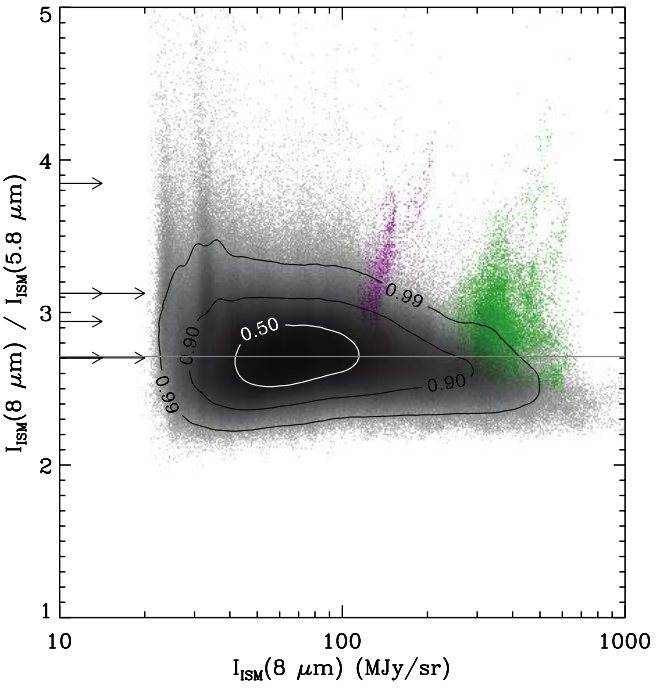

Fig. 5.—The 8/5.8 μm color vs. brightness in the GC region. The shading represents the diffuse emission. Contours indicate the regions containing 50%, 90%, and 99% of the data. The solid line shows the median color (2.71) of the diffuse emission, and the arrows indicate the colors reported for six other regions of the Galactic plane by Flagey et al. (2006). The cluster of green points indicates those found in the shell around the Arches cluster (see Fig. 6), and the cluster of magenta points indicates those found in the more compact regions at higher latitudes (see Fig. 7). The large dispersion in the color at $I_{\mathrm{ISM}}(8\ \mu\mathrm{m}) < 35$ MJy sr^{-1} is from faint locations at $|b| > 0.5$, where errors in the subtraction of stellar and zodiacal backgrounds can have large effects on the colors.

3.1.3. *Shorter Wavelength Colors*

We are unable to make an analogous comparison to $I(8\ \mu\mathrm{m})/I(3.6\ \mu\mathrm{m})$ and $I(8\ \mu\mathrm{m})/I(4.5\ \mu\mathrm{m})$ colors measured by Flagey et al. (2006) because the very bright and confusing unresolved stellar background toward the GC overwhelms nearly all diffuse ISM emission at the shorter wavelengths. Point source–subtracted images (see Ramírez et al. 2008) provide some aid in distinguishing nonstellar 3.6 and 4.5 μm emission, but all such regions appear to be H II regions and PDRs associated with specific heating sources, rather than diffuse ISM heated by the ISRF.

3.2. *Unusual Emission Regions*

Along the Galactic plane, there are a few large ($\gtrsim 4'$) emission features that stand out in the $I(8\ \mu\mathrm{m})/I(5.8\ \mu\mathrm{m})$ color map with unusually red colors. The largest of these is an oblong shell-like structure centered on the Arches cluster, which contains ~200 stars with masses >20 $M_\odot$ (Figer et al. 2002). The shell is much more clearly delineated by the color of its emission than by the 8 μm surface brightness (Fig. 6, *top row*). On the north, this shell seems bounded by the innermost of the thermal radio arches surrounding the cluster. The shell is only faintly discernible in the shorter wavelength colors. A similar but smaller region appears near the Quintuplet cluster (Fig. 6, *middle row*), which is comprised of a cluster of hot O/B and WR stars responsible for ionizing the nearby ISM (Cotera et al. 1996). However, the five cocoon stars (Moneti et al. 2001) that give this cluster its name are so bright at IRAC wavelengths that artifacts from these sources obscure much of this excess.

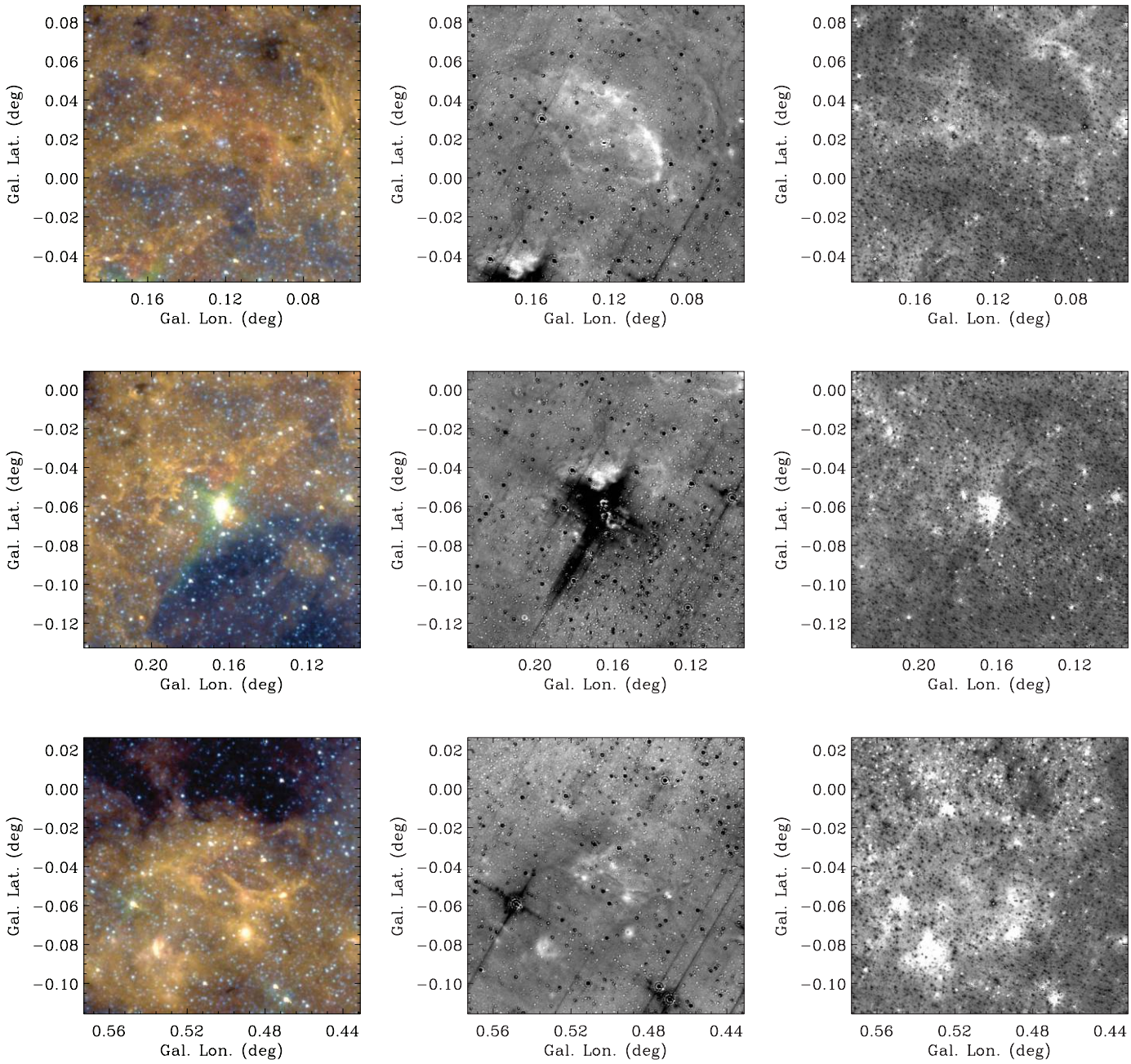

FIG. 6.—Unusually red regions at low latitudes: the Arches cluster region (*top row*), Quintuplet cluster region (*middle row*), and Sgr B1 region (*bottom row*). *Left column*: 4.5, 5.8, and 8 μm emission logarithmically scaled as blue, green, and red, respectively. *Middle column*: $I_{\rm ISM}(8\ \mu{\rm m})/I_{\rm ISM}(5.8\ \mu{\rm m})$ linearly scaled in the range 2.0–4.0. *Right column*: $I(4.5\ \mu{\rm m})/I(3.6\ \mu{\rm m})$ linearly scaled in the range 0.5–1.5. (In the middle and right columns, lighter shades indicate redder colors.) All these regions contain extended emission that, despite being relatively faint, is very red in $I_{\rm ISM}(8\ \mu{\rm m})/I_{\rm ISM}(5.8\ \mu{\rm m})$ colors but not in $I(4.5\ \mu{\rm m})/I(3.6\ \mu{\rm m})$ colors.

There are weaker indications of unusually red emission in the Sgr B1 region as well (Fig. 6, *bottom row*). The redder infrared emission is associated with 5.8 and 8 μm counterparts of the "ionized bar" and "ionized rim" features identified in 3.6, 6, and 20 cm radio observations by Mehringer et al. (1992). Unlike the Arches and Quintuplet regions, however, the most luminous stars here are not grouped in a tight, easily identified cluster but are apparently dispersed throughout the volume.

All these extended red regions (the vicinities of the Arches and Quintuplet clusters and Sgr B1) can be distinguished in Figure 5 as the cluster of outlier points at 250 MJy sr^{-1} $< I(8\ \mu{\rm m}) <$ 1000 MJy sr^{-1} and $I_{\rm ISM}(8\ \mu{\rm m})/I_{\rm ISM}(5.8\ \mu{\rm m}) > 3.2$. We expect that, as with the compact H II regions, the excessively red emission is caused by thermal emission from very warm dust in strong radiation fields. However, in these cases the excess emission appears over a wider region because of the larger number of luminous stars in these clusters and lower column densities around these more evolved systems allowing a strong radiation field to propagate over a larger volume.

The Pistol Nebula on the edge of the Quintuplet cluster is a different type of red emission region. The 8 μm IRAC data reveal an entire shell or bubble around the Pistol star, with a diameter of $\sim 22''$ (almost 1 pc at the distance of the GC). The brighter portion of this bubble is likely being ionized by the hot stars in the Quintuplet cluster (Figer et al. 1999). The Pistol Nebula exhibits the most extremely red $I_{\rm ISM}(8\ \mu{\rm m})/I_{\rm ISM}(5.8\ \mu{\rm m})$ color in the region, as it is only marginally distinguishable at 5.8 μm. (The 5.8 μm emission is very difficult to quantify because of

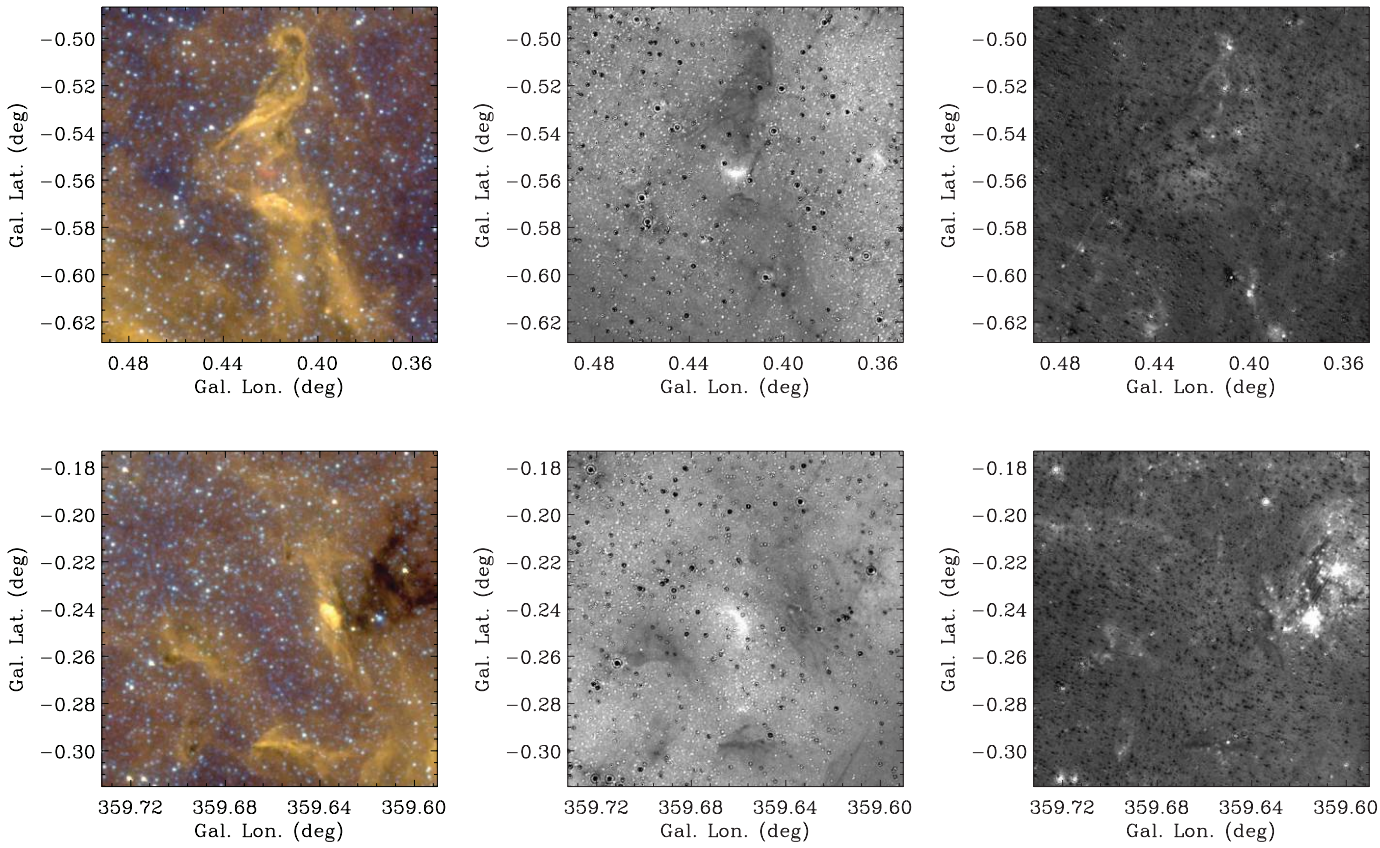

FIG. 7.—Unusually red regions at high latitudes: IRAS 17456−2850 (*top row*) and IRAS 17425−2920 (*bottom row*). *Left column*: 4.5, 5.8, and 8 μm emission logarithmically scaled as blue, green, and red, respectively. *Middle column*: $I_{\rm ISM}(8\ \mu{\rm m})/I_{\rm ISM}(5.8\ \mu{\rm m})$ linearly scaled in the range 2.0–4.0. *Right column*: $I(4.5\ \mu{\rm m})/I(3.6\ \mu{\rm m})$ linearly scaled in the range 0.5–1.5. (In the middle and right columns, lighter shades indicate redder colors.) Both these *IRAS* sources are faint and extended but very red in $I_{\rm ISM}(8\ \mu{\rm m})/I_{\rm ISM}(5.8\ \mu{\rm m})$ colors.

strong banding artifacts from the extremely bright stars of the Quintuplet cluster.) Physically, the emission from this region is associated with the ejecta from a single star (the Pistol star) which is a luminous blue variable (Figer et al. 1998). In this case, *ISO* spectroscopy of the nebula already suggests that the 8 μm excess is due to a relatively red continuum (with deep silicate extinction at 10 μm) and lack of PAH emission (Moneti et al. 1999). The [Ar II] 6.99 μm line is the strongest line between 5 and 10 μm, but it is not bright enough to be the dominant cause of the red color. There are no other similar (bright, sharply defined, and very red) circumstellar bubbles evident in our GC survey. Two partial shells around massive stars near the GC have been identified by Mauerhan et al. (2007). Neither of these shells exhibit especially red $I_{\rm ISM}(8\ \mu{\rm m})/I_{\rm ISM}(5.8\ \mu{\rm m})$ color, although in one case red emission is present interior to the shell.

There are only two extended ($\sim$20″) emission sources >0.1° away from the Galactic plane that show strong 8 μm excesses (Fig. 7). Unlike the bright compact H II regions, these sources are not very bright at 8 μm, and thus even fainter or absent at 5.8 μm. However, both brighten rapidly at longer wavelengths, are detected as *IRAS* point sources at 25 μm (IRAS 17456−2850 and IRAS 17425−2920), and are visible in the *MSX* band E (21.3 μm) images. Both are located near (in projection) extended star-forming regions (RCW 137 in the case of IRAS 17425−2920) with strong cirrus emission and IRDCs. Both are slightly extended and bowed or arced. Neither source contains an obvious point source nor has a known energizing star in the crowded field. IRAS 17425−2920 does not appear in the 1616 GHz radio maps of the Sgr C region (Liszt & Spiker 1995). The characteristics and locations of these sources on the outskirts of active star-forming regions suggest that these sources represent a very early stage of star formation. Alternately, they could represent local heating by a fully formed star that is interacting with an otherwise quiescent molecular or neutral cloud. A third option is that these objects indicate some sort of shock phenomenon and the unusual colors are the result of strong line emission. For example, the candidate SNR SSTGFLS J222557+601148 exhibits only line emission with no continuum (Morris et al. 2006). This particular object is bright in the MIPS 24 μm band by virtue of a strong [O IV] 26 μm line but is invisible to IRAC. In the Cas A SNR, [Ar II] at 6.99 μm can contribute 40% of the emission in the IRAC 8 μm band (Ennis et al. 2006). Outside of our survey area at $l = 7^\circ$, Rho et al. (2006) detect a similar source in the IRAC and MIPS observations of the Trifid Nebula (Rho et al. 2006). The region they call "Trifid Junior" lies north of the H II region and the reflection nebula. It is a small arc of emission at 24 μm which can just barely be seen at 8 μm and is absent at 5.8 μm. The general appearance of the local ($\sim$5′) vicinity is very similar to that of IRAS 17425−2920.

3.3. *Molecular Emission: A Dearth of* 4.5 μm *Excess Sources*

Molecular outflows from young stellar objects are often dramatically highlighted in IRAC images because of CO and H_2 emission lines that are especially strong in the 4.5 μm IRAC band (e.g., Smith et al. 2006). This wavelength is usually depicted as green in multicolor images, and such outflows are therefore recognized by their green colors in such images. While some star-forming regions can contain dozens of outflow sources (e.g., Orion, DR 21, and NGC 1333), there is only a single small source that is strong

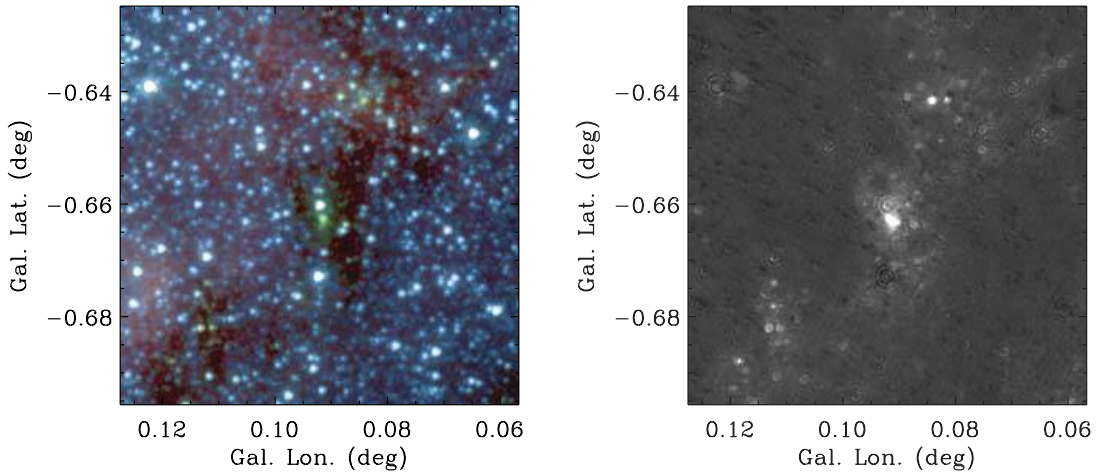

FIG. 8.—*Left*: 3.6 (*blue*), 4.5 (*green*), and 5.8 (*red*) μm emission centered on 2MASS 17482532−2911590. There is a slightly extended diffuse feature just $\sim 10''$ south of the point source. This extended emission is relatively strong at 4.5 μm, as indicated by the green color and a high $I(4.5\ \mu\text{m})/I(3.6\ \mu\text{m})$ ratio (shown in the right panel on a linear range of 0–3). This color is often an indication of molecular emission in outflows or Herbig-Haro objects associated with very young stars.

at 4.5 μm *and* has a jetlike morphology within our GC survey (Fig. 8). There are dozens of other sources that also have 4.5 μm excesses, but these are unresolved or only slightly diffuse and usually within or near more extended regions of bright 8 μm emission. Many of these may be outflows from young stellar objects that are too distant or intrinsically small to be resolved. Further discussion of these sources can be found in Yusef-Zadeh et al. (2007b).

In several of the large, more local star-forming regions at higher Galactic latitudes there are broad diffuse regions of relatively enhanced 4.5 μm emission [e.g., near $(l, b) = (0.48^\circ, -0.67^\circ)$]. Rather than being an indication of molecular emission, these may be cases where we spatially resolve an H II region from its surrounding PDR. The recent study of M17 by Povich et al. (2007) shows that the absence of PAH emission within the H II region where a strong extreme UV radiation field is present is well correlated with an apparent excess at 4.5 μm. Thus, the excess is really only a decrease in the strength of the PAH features that dominate the 5.8 and 8 μm emission (and to a lesser degree 3.6 μm emission) in the surrounding PDR.

3.4. *Unseen Objects*

There are six known SNRs (Sgr A East, G0.3+0.0, G0.9+0.1, G1.0−0.1, G359.0−0.9, and G359.1−0.5; Green 2006) that lie at least partially within our survey regions, but at 3.6–8 μm none of these are visible by either their intensity or color. This is not unexpected given the high degree of confusion and the fact that SNRs are often difficult to distinguish in the infrared even with $2''$ spatial resolution. A thorough examination of the IRAC GLIMPSE survey ($10^\circ < |l| < 65^\circ$) by Reach et al. (2006) found IRAC counterparts for only 18 of 95 SNRs. Those that were detected are undergoing strong interactions with dense, often molecular, clouds. The lack of detections in our survey means that none of the six SNRs toward the GC is undergoing a strong enough interaction to be visible above the brightest background confusion in the Galaxy. The southern portion of IC 443 is a well-studied example of a SNR/molecular cloud interaction (e.g., Cesarsky et al. 1999). Emission with the same surface brightness as IC 443 (AOR ID = 4422912 and 4423168) could be distinguished at higher latitudes but would be lost in the confusion at $|b| \lesssim 0.2^\circ$. Fainter examples of shocked molecular emission such as W44 (Reach et al. 2006) would likely be lost in the confusion at any location within our survey.

The enigmatic infrared source known as AFGL 5376 does not show any distinct emission at any IRAC wavelength, despite being a bright extended source at $\sim$24 μm wavelengths (Uchida et al. 1990, 1994; Law 2007). We do note that there are several small IRDCs and filaments [in the vicinity of $(l, b) = (0.7244^\circ, -0.4759^\circ)$] that can been seen in extinction against the 24 μm emission of AFGL 5376, as well as the general 3.6–8 μm background. There is also no particular correlation between the diffuse infrared emission and the nonthermal radio filament and threads that are present in the GC region (Yusef-Zadeh et al. 2004; Stolovy et al. 2006; S. Stolovy et al. 2008, in preparation).

4. DISCUSSION

Overall, the GC exhibits homogenous IRAC colors that are quite similar to those of other regions of the Galactic plane. Such a uniform $I_{\rm ISM}(8\ \mu\text{m})/I_{\rm ISM}(5.8\ \mu\text{m})$ color for the diffuse emission indicates that there is little reddening associated with extinction at these wavelengths, despite evidence for highly variable extinction in the form of IRDCs and extinction measurements made at shorter wavelengths (e.g., Gosling et al. 2006). This is expected given the flattening of the Galactic extinction curve (Lutz et al. 1996; Indebetouw et al. 2005; Flaherty et al. 2007). Even if the extinction did produce reddening, it would be extremely unlikely for the line-of-sight reddening to be correlated with variation in the intrinsic color of the emission to produce such an overall uniform color.

The uniform colors are also evidence that the emission spectrum is largely independent of the local and global locations and environments. This strongly suggests that emission from PAHs dominates the diffuse ISM emission (5.8–8 μm) all the way to the GC. The relative strengths of PAH emission bands that fall within the IRAC 5.8 and 8 μm filter bandpasses are unaffected by the strength of the radiation field heating the grains over a wide range of intensities (Li & Draine 2001). Even as the ISRF strength increases toward the GC, there is no evident change in the color of the PAH emission. Figure 9 shows model spectra of the ISM emissivity normalized to the strength of the ISRF (Mathis et al. 1983), as characterized by a scale factor χ. The dust model used here is composed of PAHs and bare graphite and silicate grains (the "BARE-GR-FG" model of Zubko et al. 2004). This model is similar to those of Li & Draine (2001) but is derived via additional constraints provided by elemental abundances.

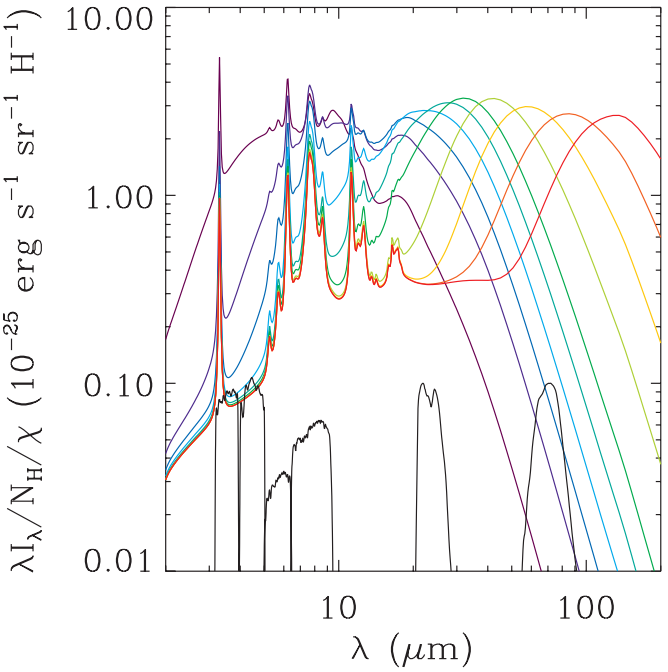

FIG. 9.—Colored curves show the emission spectra for a selected dust grain model (BARE-GR-FG from Zubko et al. 2004) subjected to radiation fields of $\chi = 10^{[0,1,2,3,4,4.5,5,5.5,6,7]}$ times the local ISRF. The black lines indicate the filter responses (arbitrarily normalized) for the four IRAC channels and the MIPS 24 and 70 μm channels. The PAH spectrum is unchanged with radiation field strength, hence the IRAC flux ratios remain unaltered until the larger, roughly equilibrium temperature grains get so warm that they encroach on the 8 μm IRAC band. Note that the continuum, not PAH emission bands, dominates the 3.6 and 4.5 μm IRAC filters. The 3.3 μm PAH feature contributes <30% of the total flux in the IRAC 3.6 μm channel for these models.

For the standard ISRF ($\chi = 1$), most emission at $\lambda < 60$ μm is from very small grains ($\lesssim$0.01 μm) and PAHs. These grains have a low heat capacity and are heated to high temperatures by absorption of a single photon. They radiate that energy quickly and cool below equilibrium temperatures before the next energetic photon hits. Thus, for these stochastically heated particles, the grains do not get any warmer as the radiation field increases; they only go through the same temperature spikes more frequently. Therefore, the spectrum normalized by χ remains roughly constant. This is especially evident at $\lambda < 10$ μm. Larger grains ($\gtrsim$0.01 μm) have higher heat capacities and absorb photons frequently enough that they radiate at their equilibrium temperatures. For the local ISRF ($\chi = 1$), this thermal emission peaks at $\sim$150 μm. As χ increases, the larger grains get warmer and the thermal emission moves to shorter wavelengths. Eventually, when $\chi \gtrsim 10^4$, the thermal emission begins to enter the 8 μm IRAC band. At this point the IRAC colors can be affected.

In Figure 10 we plot $I_{\rm ISM}(8\ \mu{\rm m})/I_{\rm ISM}(5.8\ \mu{\rm m})$ predicted by the models of a function of radiation field strength. The figure shows that the BARE-GR-FG model is consistent with the observed $I_{\rm ISM}(8\ \mu{\rm m})/I_{\rm ISM}(5.8\ \mu{\rm m})$ mean color as long as $\chi \lesssim 10^4$. It is also evident that while the color initially reddens as the thermal emission from the hot dust enters the 8 μm band, the color begins getting bluer when the thermal emission pushes into the 5.8 μm band as well. However, the reddest colors attained by this model (at $\chi \sim 10^5$) are not nearly red enough to explain the unusually red regions that we identify in the GC region (§ 3.2). Alternatively, if the PAH component is removed from the BARE-GR-FG model, then at $\chi \sim 10^5$ the color of the emission can be sufficiently red to match the observations. At $\chi \lesssim 10^4$, the colors of the emission would be much bluer than observed if PAHs were generally absent from the ISM in the GC. Qualitatively similar results are obtained from the Draine & Li (2007) dust models, which include a parameter ($q_{\rm PAH}$) that characterizes the relative abundance of PAHs.

The red shell around the Arches cluster provides a nice example of a region with a locally strong radiation field. Figer et al. (2002) have estimated the luminosity of the Arches cluster as $10^{7.8}\ L_\odot$. The extended red shell has a radius of $\sim$100″, or 3.9 pc. Thus, the energy density at the outer edge of this shell is $\sim 4.4 \times 10^{-9}$ erg cm^{-3}. Compared to the nominal strength of the local ISRF, 7×10^{-13} erg cm^{-3} (Spitzer 1978), we find that $\chi \sim 6300$ at the edge of the shell. This value of χ indicates that we should indeed expect to see emission with red $I_{\rm ISM}(8\ \mu{\rm m})/I_{\rm ISM}(5.8\ \mu{\rm m})$ colors in the vicinity of the Arches cluster, and that the region of red emission cannot be much larger than what is observed.

The red emission region near the Quintuplet cluster is related to a similarly enhanced radiation field. This region corresponds to the portion of the Sickle that is nearest the Quintuplet cluster.

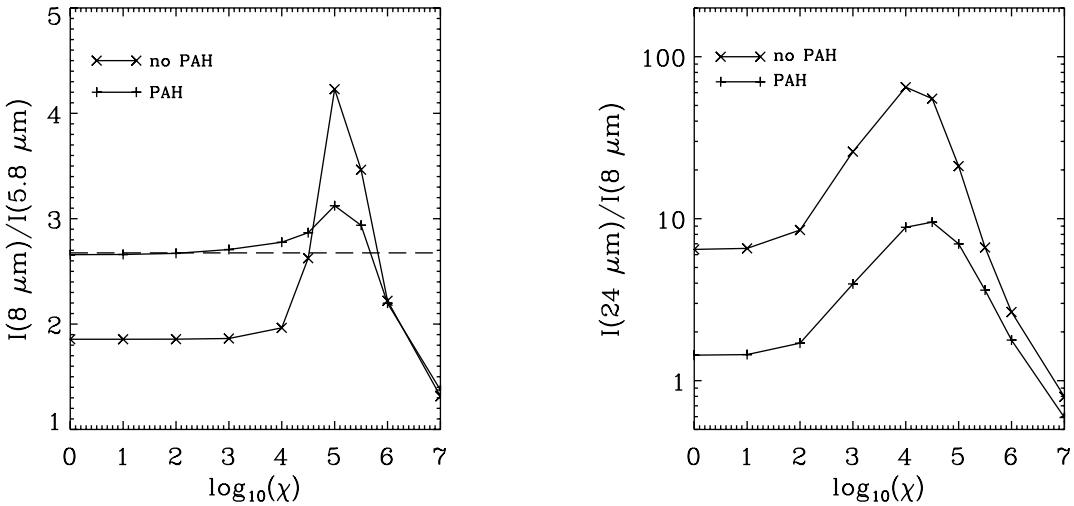

FIG. 10.—*Left*: Quantifying the $I(8\ \mu{\rm m})/I(5.8\ \mu{\rm m})$ ratio for the dust models shown in Fig. 9. The dashed line shows the median ratio over the whole GC region. *Right*: Corresponding $I(24\ \mu{\rm m})/I(8\ \mu{\rm m})$ ratio. Involving longer wavelengths, this color is more sensitive to changes in the cooler, larger dust grains and lower values of the radiation field χ.

Spectroscopy of this region by Simpson et al. (1997, 2007) reveals gas in a state of high excitation, consistent with radiation fields of $\chi > 10^3$. Calculations by Rodríguez-Fernández et al. (2001) indicate that the Quintuplet cluster will fill a smaller volume with a strong radiation field than the Arches cluster. This is in agreement with the smaller extent of the red emission in the vicinity of the Quintuplet cluster compared to the Arches cluster (Fig. 6). In particular, the extent of the radiation field strong enough to cause redder $I_{\rm ISM}(8\ \mu{\rm m})/I_{\rm ISM}(5.8\ \mu{\rm m})$ colors does not reach to the (Galactic) southern end of the radio arc bubble. This is consistent with the fact that while 20–25 μm observations (*IRAS*, *MSX*, and MIPS) show a complete bubble, the portions more distant from the Quintuplet cluster do not exhibit unusually red $I_{\rm ISM}(8\ \mu{\rm m})/I_{\rm ISM}(5.8\ \mu{\rm m})$ colors. Comparison of the spectroscopic results of Simpson et al. (2007) indicates that the $I_{\rm ISM}(8\ \mu{\rm m})/I_{\rm ISM}(5.8\ \mu{\rm m})$ color is fairly well correlated (correlation coefficient $r > 0.6$) with the continuum intensity at $\lambda > 10\ \mu$m and with H I 7–6 12.37 μm, [Ne II] 12.81 μm, [P III] 17.89 μm, [S III] 18.71, 33.48 μm, and [S IV] 10.51 μm. The correlation of the $I_{\rm ISM}(8\ \mu{\rm m})/I_{\rm ISM}(5.8\ \mu{\rm m})$ color with the $\lambda > 10\ \mu$m continuum color or with line ratios is weaker. An exception is that the correlation with [Si II] 34.83 μm/[Fe II] 26 μm (or 17.94 μm) is quite strong, $r > 0.75$. This is rather surprising, as both species have similar ionization potentials and would be similarly affected by depletion into (or destruction of) dust grains.

5. SUMMARY

Our *Spitzer* IRAC survey of the Galactic center (GC; Stolovy et al. 2006; S. Stolovy et al. 2008, in preparation) reveals prominent 5.8 and 8 μm emission from the ISM in the central $\sim$200 pc of the Galaxy in unprecedented detail. The infrared emission is loosely associated with molecular emission from the CMZ and several times brighter than infrared emission elsewhere in the Galactic plane. In general, the $I_{\rm ISM}(8\ \mu{\rm m})/I_{\rm ISM}(5.8\ \mu{\rm m})$ color of the emission is very uniform across the CMZ and similar to that seen in other parts of the Galactic plane (e.g., Flagey et al. 2006). Clearly, we cannot infer too much from a single color, given the large number of parameters that can be adjusted for the dust models used to interpret the emission. However, we can generally conclude that the predominant uniformity of the observed $I_{\rm ISM}(8\ \mu{\rm m})/I_{\rm ISM}(5.8\ \mu{\rm m})$ color in the GC implies that (1) the emission is dominated by PAHs, (2) the general ISRF in the central 200 pc of the Galaxy does not reach extreme values ($\chi \lesssim 10^4$), and (3) the interstellar extinction law at these wavelengths is flat (e.g., Indebetouw et al. 2005; Flaherty et al. 2007), leading to no significant reddening despite obvious cases of locally high extinction.

There are several extended regions that exhibit much redder than average $I_{\rm ISM}(8\ \mu{\rm m})/I_{\rm ISM}(5.8\ \mu{\rm m})$ colors despite not being especially bright. Red regions around the Arches cluster, the Quintuplet cluster, and Sgr B1 are apparently produced by a combination of locally strong radiation fields ($\chi \gtrsim 10^4$) and a lack of PAHs (perhaps a consequence of the strong radiation field). Other very red regions that are more compact and further from the Galactic plane appear to be associated with the onset of star formation, although they do not appear to contain any detectable point sources.

This work is based on observations made with the *Spitzer Space Telescope*, which is operated by the Jet Propulsion Laboratory, California Institute of Technology, under a contract with NASA. Support for this work was provided by NASA through an award issued by JPL/Caltech. This research has made use of the NASA/IPAC Infrared Science Archive, which is operated by the Jet Propulsion Laboratory, California Institute of Technology, under contract with the National Aeronautics and Space Administration. We thank the referee for pointing out the nonnegligible influence of the 4.5 μm ISM emission in our analysis.

Facilities: Spitzer (IRAC)

APPENDIX

DATA REDUCTION DETAILS

A1. POST-BCD PROCESSING

The BCDs are single frames (exposures) calibrated with the standard calibration data applied by the *Spitzer* Science Center (SSC) pipeline. While on average this calibration is quite good, in some cases the state of the IRAC detectors may be different from what the standard calibration assumes. Thus, the BCDs can still contain some types of instrumental artifacts, and the individual frames may not blend smoothly into a large mosaicked image, especially when that image incorporates multiple AORs.

One significant artifact in the 3.6 and 4.5 μm channels is "column pulldown." This is an electronic artifact that induces low intensities in detector columns coincident with bright (usually saturated) sources. A standard correction was applied to individual BCD frames for the 3.6 and 4.5 μm channels. This greatly mitigated the effect but did not reduce it to undetectable levels. A similar correction for banding was applied to 8 μm BCD frames to eliminate excess intensity in detector rows containing very bright sources. The 5.8 μm data could have benefited from such corrections in both detector rows and columns. However, the character of the artifact is sufficiently different from the behavior at 8 μm that attempts at correcting 5.8 μm banding were not successful enough to apply them in an automated way. Thus, these artifacts remain and are a source of systematic error in particular regions where saturated sources are clustered.

The BCD frames for each AOR were self-calibrated using the procedure described by Fixsen et al. (2000). This procedure uses the bright infrared background emission (combined zodiacal light and Galactic emission) as a calibration source. The background is not uniform, but it is stable. Thus, when the dithering and mapping place different detector pixels on the same sky location, the resulting values for *properly* calibrated data should be the same, apart from a random noise variation from Gaussian detector noise and Poisson photon shot noise. Not all detector pixels observe a single sky location, but with a large data set such as ours, if two different detector pixels did not observe a common sky location, then there is an intermediate pixel (or a chain of several such pixels) that has observed at least one sky location in common with each of the original two pixels. Through such intercomparisons, the relative calibrations of each detector pixel can be determined. This is solved using a linear least-squares algorithm. In the framework of this procedure the

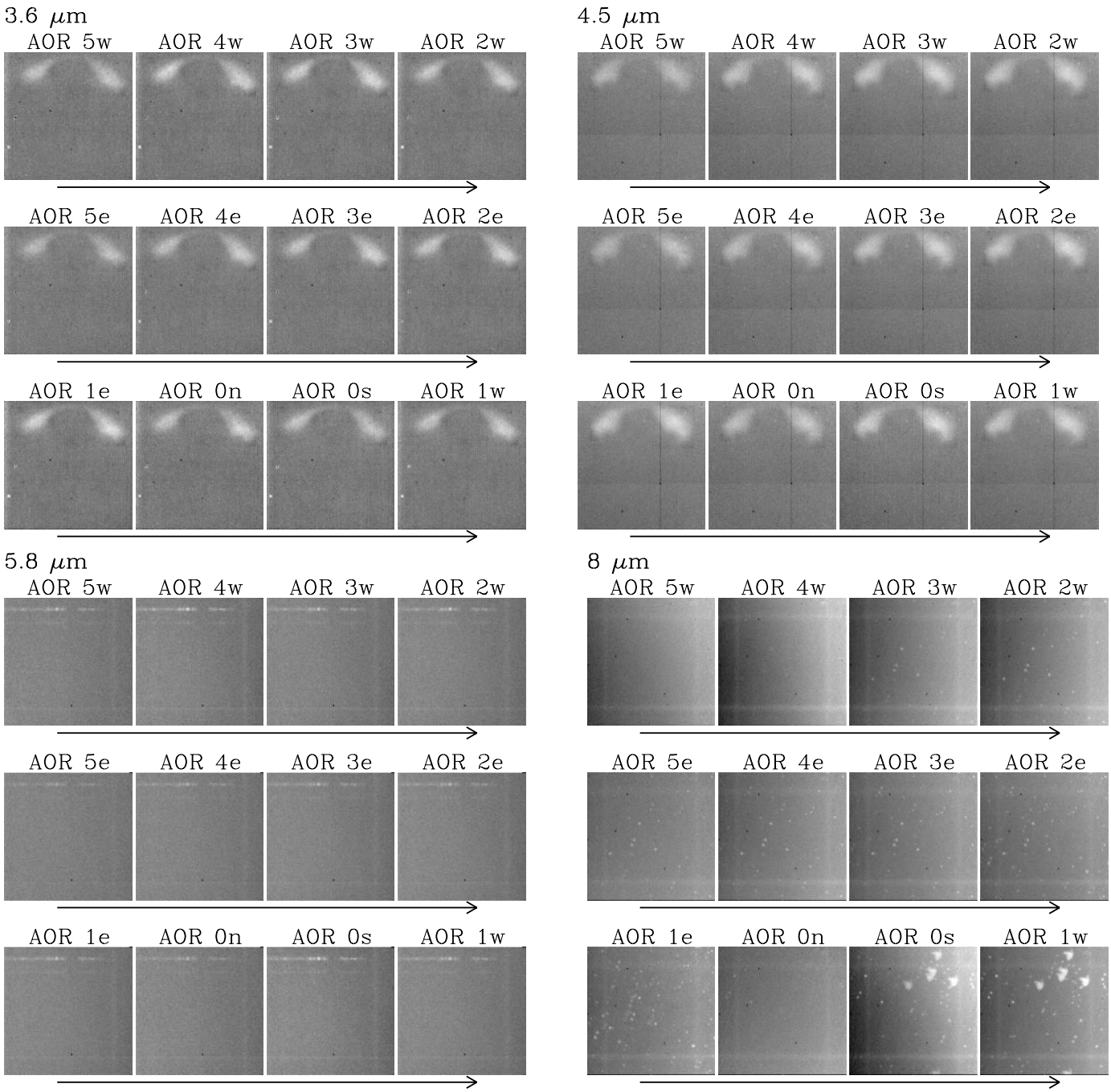

FIG. 11.—Images of the offsets (F^p) derived for each AOR in a time-ordered sequence. These show the diffuse stray light artifacts that remained in the BCD and the accumulation of long-term latent images at 8 μm. The last three AORs (0n, 0s, and 1w) were separated from the first by a downlink and anneal, which cleared previous long-term latent images. The Sgr A region creates strong latent images during AOR 0s which then remain throughout AOR 1w. Display ranges are -2 to 2, -2 to 2, -5 to 5, and -4 to 4 MJy sr^{-1} for 3.6–8 μm, respectively.

data (D^i; i.e., each pixel of each BCD frame) are modeled as the sum of the true sky intensity (S^α at sky coordinates α), a fixed detector offset (F^p as a function of detector pixel p), and a variable offset (F^q a single value for all pixels of frame q),

$$D^i = S^\alpha + F^p + F^q. \tag{A1}$$

The least-squares self-calibration allows us to determine the offset terms in the model (i.e., the proper detector calibration) and then invert equation (A1) to derive the true sky intensity, S^α, from the data, D^i. The images of the fixed detector offsets (F^p) are shown in Figure 11 for each IRAC channel and each AOR. For the 3.6 and 4.5 μm data, the obvious feature is the diffuse stray light "butterfly wing" pattern at the top of the detector. This feature represents the integrated stray light of all the sources of the bright unresolved background, which is not effectively removed through the standard BCD calibration. The amplitude of this artifact is small and not directly evident in the single BCD frames or the mosaics, but if left uncorrected it will induce artifacts in the ratio of 3.6/4.5 μm emission as shown in Figure 12. This figure

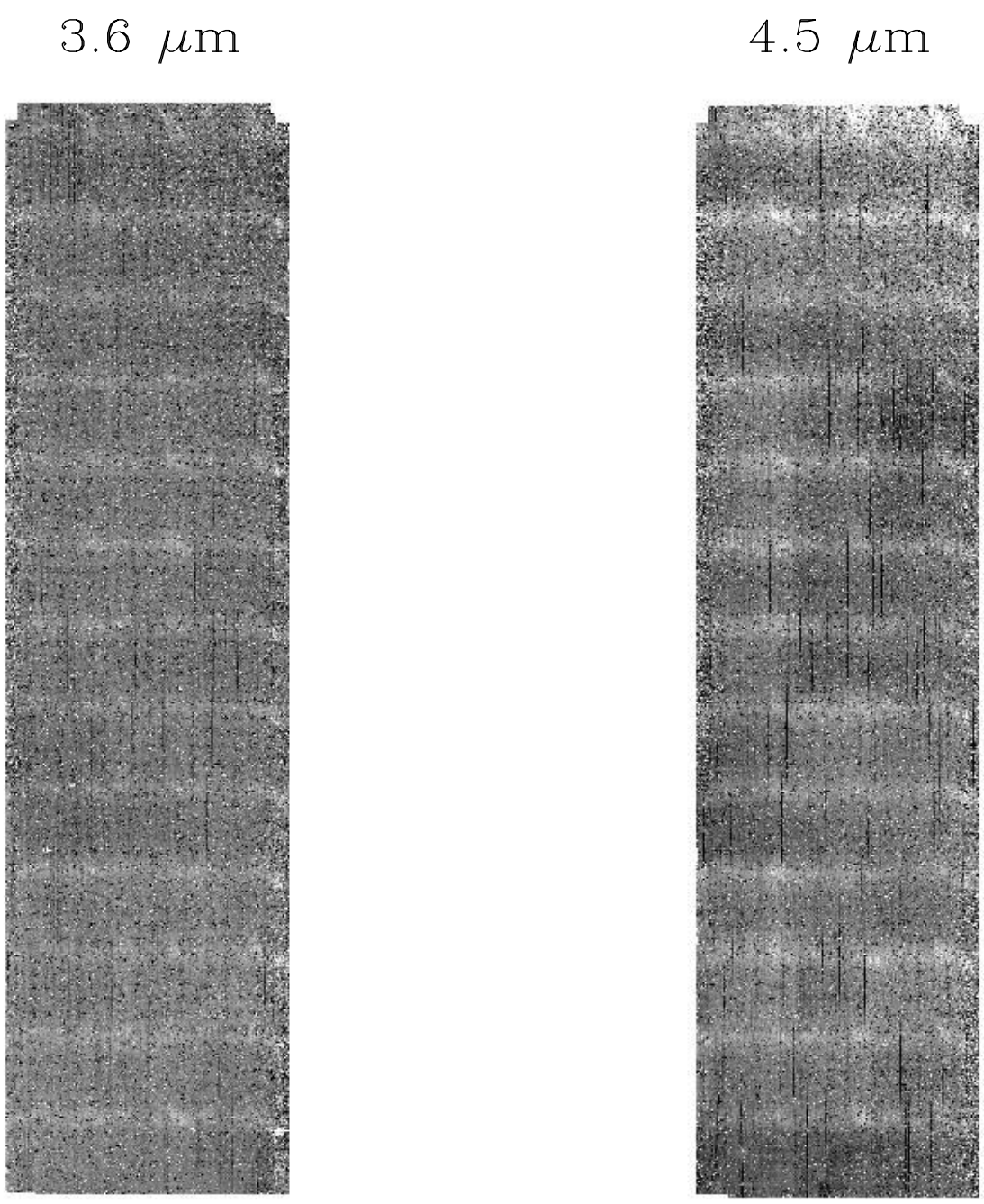

FIG. 12.—Ratios of standard post-BCD mosaics to our self-calibrated BCD mosaics for one AOR strip of the survey (AOR ID = 13371648) at 3.6 μm (*left*) and 4.5 μm (*right*). The display range is 0.9–1.2. The light horizontal bands indicate the regions that are affected by the diffuse stray light in the post-BCD mosaics. These artifacts are present in the ratio of 3.6/4.5 μm post-BCD mosaics, but not in ratios of our self-calibrated mosaics. The dark vertical lines illustrate the changes due to the application of the column pulldown correction.

also illustrates that the column pulldown correction is not entirely effective at both 3.6 and 4.5 μm for the very brightest sources, but the pulldown correction usually does improve the data for weaker, more frequent cases. The fixed detector offsets for the 5.8 and 8 μm channels also show (weakly) the diffuse stray light patterns for these channels (Fig. 11). In addition, the 8 μm results clearly show the accumulation of latent images from bright sources, the clearing of these after an anneal, and the further accumulation of new latent images. The strong latent images acquired at 8 μm during AOR 0s are from the central cluster at Sgr A. The relative strength and extent of the latent image indicate that the Sgr A cluster is clearly the highest density of bright sources in our survey.

The variable detector offset (F^q) is illustrated in Figures 13 and 14. The time sequence of these shows a regular variation each time one of the AOR strips crosses the brightest part of the Galactic plane. For the InSb detectors used at 3.6 and 4.5 μm, $|F^q| \lesssim 0.5$ MJy sr^{-1} and is usually much smaller than the observed sky intensities (which do not include zodiacal light), as shown in Table 1. The variable offsets can be much larger for the 5.8 and 8 μm detectors, as seen in Figure 13. Here the variable offsets are correcting for any residual errors in the "first-frame" effect (a change in detector offset as a function of time since the preceding frame) and more noticeably for detector droop (where the detector offset changes as a function of the total illumination on the detector). Figure 15 shows the ratio of our mosaic compared

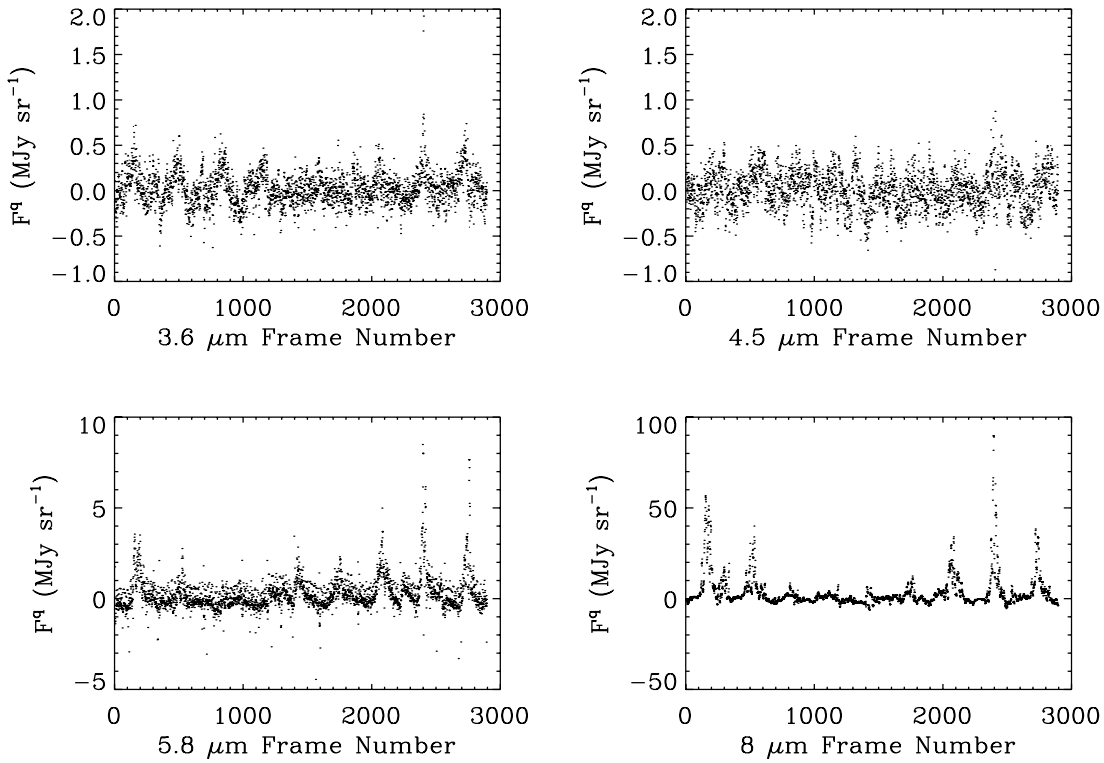

FIG. 13.— Variable offsets per frame (F^q) for each channel plotted in a time-ordered sequence. The 5.8 and 8 μm channel offsets are relatively large and well correlated with the local sky intensity, as revealed by mapping the offsets (Fig. 14).

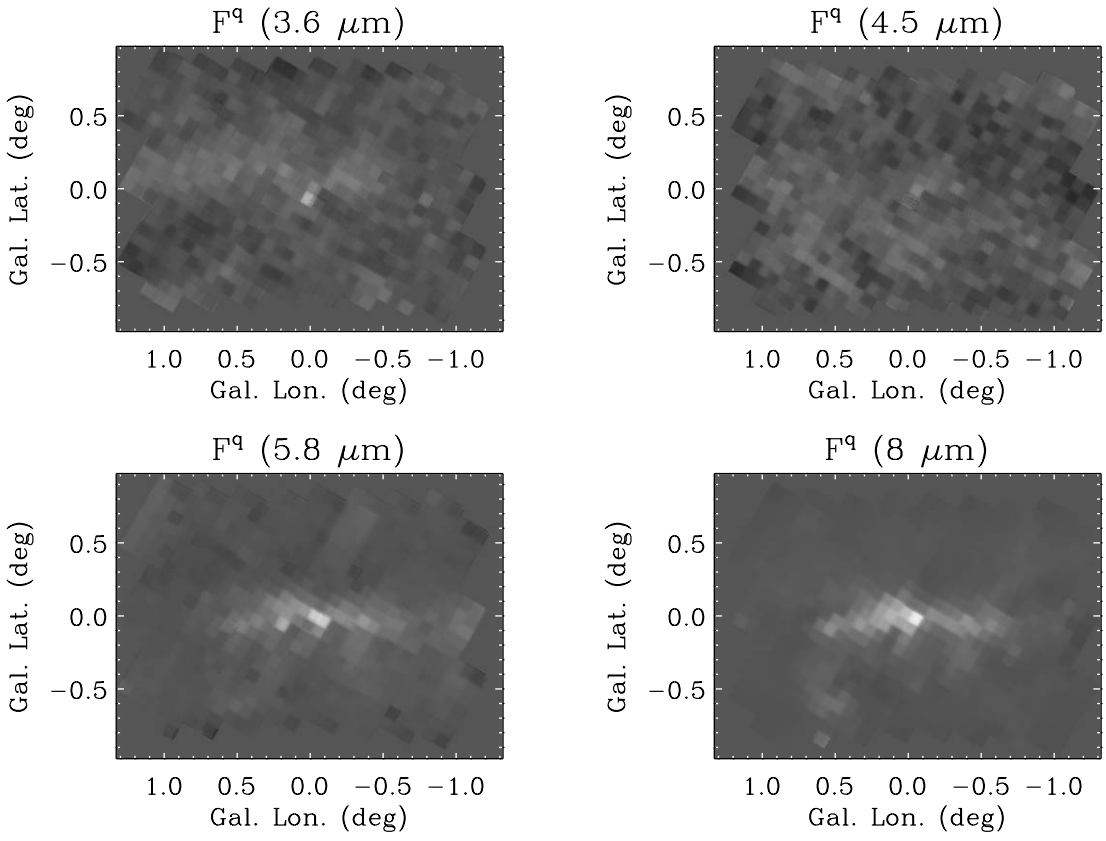

FIG. 14.— Variable offsets per frame (F^q) for each channel mosaicked into images in Galactic coordinates. The linear gray-scale ranges are the same as in Fig. 13. The 5.8 and 8 μm channel offsets are relatively large and well correlated with the local sky intensity, and thus these maps resemble very low resolution images of the GC region.

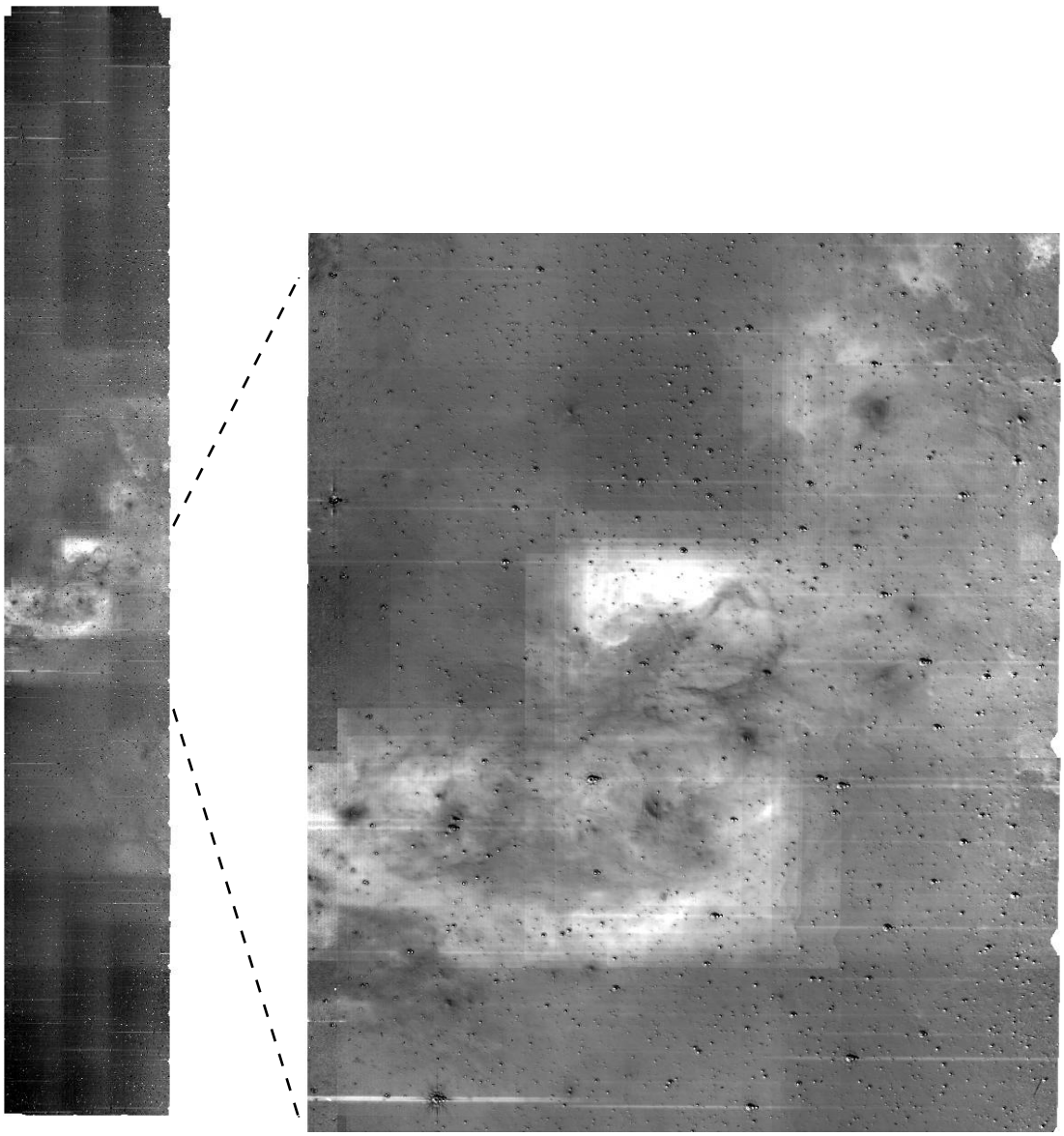

FIG. 15.—Ratio of the standard post-BCD mosaic to our self-calibrated BCD mosaic for one AOR strip of the survey (AOR ID = 13368320) at 8 μm. The display range is 0.8–1.3. This ratio highlights the corrections made by the fixed and variable offsets derived via self-calibration. Some of the sharpest frame boundaries evident here (in the expanded view) are visible in the standard post-BCD mosaics but not in the self-calibrated mosaics. The bright region around Sgr B1 is at the center of this $0.25^\circ \times 1.75^\circ$ strip. The lack of banding correction in the post-BCD mosaic causes the horizontal streaks at the locations of bright stars.

to a standard post-BCD pipeline mosaic for one strip of our survey (AOR ID = 13368320) at 8 μm. This ratio clearly shows artifacts at the frame boundaries, indicating offset errors in one (or both) of the mosaics. These errors are largest at the bright emission through the center of the strip at $b = 0$, especially for the 8 μm channel. The facts that (1) the frame seams are faintly visible in the post-BCD mosaic and not our self-calibrated versions and (2) the subsequent science analysis reveals no similar discrepancies in the ratios of 5.8-to-8 μm emission despite independently derived corrections for each channel indicate that the variable offsets derived from the self-calibration are appropriate. In other words, the self-calibration procedure does remove artifacts from the images which would otherwise cause systematic errors when comparing intensities at different wavelengths.

A2. EXTENDED SOURCE CALIBRATION AND ZODIACAL LIGHT

The absolute calibration of IRAC is based on the photometry of point sources in a fixed size aperture. In the present study, we are interested in the surface brightness of extended emission. Therefore, we have applied extended source corrections to the data used in this analysis. Specifically, the factors used here are 0.944, 0.937, 0.772, and 0.737 at 3.6, 4.5, 5.8, and 8 μm, respectively (Reach et al. 2005; Cohen et al. 2007).

Accurate determination of the colors of diffuse emission also relies on having properly subtracted any instrumental offsets. The major difficulty in measuring the correct instrumental offset is that IRAC does not use its shutter to take dark frames. Instead, "skydarks" (observations at a dark location near the north ecliptic pole) are used in the pipeline to remove instrumental offsets. This works well as

long as the instrumental offsets remain stable between the time the skydarks are measured and the science data are observed. IRAC's 5.8 μm channel shows the greatest instabilities in its offsets. The lack of constraints that would be provided by true dark frames also leads to an offset degeneracy in the self-calibration of these data. Inspection of equation (1) reveals that the procedure is insensitive to an arbitrary offset to the derived sky intensity S^{α} as long as the same offset is subtracted from the derived instrumental offset F^{p} (or F^{q}).

Finally, for measurement of the intensity and color of diffuse Galactic emission, the zodiacal light foreground also must be subtracted. The zodiacal light must be estimated via a model. The model used for *Spitzer* is derived from the Kelsall et al. (1998) model of the zodiacal light emission as observed by the DIRBE instrument on the *COBE* spacecraft. The model is estimated to be accurate to ~2%; however, larger unrecognized systematic errors may be present. Its use for IRAC data requires interpolation to IRAC's wavelengths and, more significantly, extrapolation from the view in Earth orbit to the view from *Spitzer*'s location several tenths of an astronomical unit away from Earth. In addition, because of the skydark subtraction, the zodiacal light must be known along the line of sight to the north ecliptic pole, as well as toward the GC. Thus, the zodiacal light intensity we subtract from the mosaic images is the difference between that estimated for the GC observations and that of the skydark observations. This is calculated from the mean values of the ZODY_EST and SKYDRKZB keywords in the BCD headers, except for the 5.8 μm channel where these keyword values are in error and are inconsistent with the model spectrum; thus, the estimates from Spot[11] are used instead for the 5.8 μm data. We do not account for the small gradient in the zodiacal light intensity.

Table 1 lists the median and mean intensities of the final GC mosaics, along with the self-calibration offsets and the estimated intensities of the zodiacal light. The zodiacal light is essentially negligible for the 3.6 and 4.5 μm data but could potentially influence the 5.8 and 8 μm results where intensities are low. The variable offset per frame (F^{q}) can reach large values, but as revealed in Figure 14, the largest values are closely confined to the Galactic plane, where intensities are also much higher than the mean or median values.

[11] See http://ssc.spitzer.caltech.edu/propkit/spot/.

REFERENCES

Altenhoff, W. J., Downes, D., Pauls, T., & Schraml, J. 1979, A&AS, 35, 23
Armstrong, J. T., & Barrett, A. H. 1985, ApJS, 57, 535
Becker, R. H., White, R. L., Helfand, D. J., & Zoonematkermani, S. 1994, ApJS, 91, 347
Benjamin, R. A., et al. 2003, PASP, 115, 953
Cesarsky, D., Cox, P., Pineau des Forêts, G., van Dishoeck, E. F., Boulanger, F., & Wright, C. M. 1999, A&A, 348, 945
Christopher, M. H., Scoville, N. Z., Stolovy, S. R., & Yun, M. S. 2005, ApJ, 622, 346
Cohen, M., et al. 2007, MNRAS, 374, 979
Cotera, A. S., Erickson, E. F., Colgan, S. W. J., Simpson, J. P., Allen, D. A., & Burton, M. G. 1996, ApJ, 461, 750
Cox, P., & Laureijs, R. 1989, in IAU Symp. 136, The Center of the Galaxy, ed. M. Morris (Dordrecht: Kluwer), 121
Draine, B. T., & Li, A. 2007, ApJ, 657, 810
Ennis, J. A., Rudnick, L., Reach, W. T., Smith, J. D., Rho, J., DeLaney, T., Gomez, H., & Kozasa, T. 2006, ApJ, 652, 376
Fazio, G. G., et al. 2004, ApJS, 154, 10
Figer, D. F., Morris, M., Geballe, T. R., Rich, R. M., Serabyn, E., McLean, I. S., Puetter, R. C., & Yahil, A. 1999, ApJ, 525, 759
Figer, D. F., Najarro, F., Morris, M., McLean, I. S., Geballe, T. R., Ghez, A. M., & Langer, N. 1998, ApJ, 506, 384
Figer, D. F., et al. 2002, ApJ, 581, 258
Fixsen, D. J., Moseley, S. H., & Arendt, R. G. 2000, ApJS, 128, 651
Flagey, N., Boulanger, F., Verstraete, L., Miville Deschênes, M. A., Noriega Crespo, A., & Reach, W. T. 2006, A&A, 453, 969
Flaherty, K. M., Pipher, J. L., Megeath, S. T., Winston, E. M., Gutermuth, R. A., Muzerolle, J., Allen, L. E., & Fazio, G. G. 2007, ApJ, 663, 1069
Gosling, A. J., Blundell, K. M., & Bandyopadhyay, R. 2006, ApJ, 640, L171
Green, D. A. 2006, A Catalogue of Galactic Supernova Remnants (Cambridge: Astrophys. Group, Cavendish Lab.), http://www.mrao.cam.ac.uk/surveys/snrs/
Hüttemeister, S., Dahmen, G., Mauersberger, R., Henkel, C., Wilson, T. L., & Martín-Pintado, J. 1998, A&A, 334, 646
Hüttemeister, S., Wilson, T. L., Bania, T. M., & Martín-Pintado, J. 1993, A&A, 280, 255
Indebetouw, R., et al. 2005, ApJ, 619, 931
Kelsall, T., et al. 1998, ApJ, 508, 44
Law, C. J. 2007, Ph.D. thesis, Northwestern Univ.
Li, A., & Draine, B. T. 2001, ApJ, 554, 778
Liszt, H. S., & Spiker, R. W. 1995, ApJS, 98, 259
Lutz, D., et al. 1996, A&A, 315, L269
Martin, C. L., Walsh, W. M., Xiao, K., Lane, A. P., Walker, C. K., & Stark, A. A. 2004, ApJS, 150, 239
Martín-Pintado, J., de Vicente, P., Fuente, A., & Planesas, P. 1997, ApJ, 482, L45
Mathis, J. S., Mezger, P. G., & Panagia, N. 1983, A&A, 128, 212
Mauerhan, J. C., Muno, M. P., & Morris, M. 2007, ApJ, 662, 574
Mehringer, D. M., Yusef-Zadeh, F., Palmer, P., & Goss, W. M. 1992, ApJ, 401, 168
Mezger, P. G. 1978, A&A, 70, 565
Moneti, A., Blommaert, J. A. D. L., Najarro, F., Figer, D., & Stolovy, S. 1999, in The Universe as Seen by *ISO*, ed. P. Cox & M. F. Kessler (ESA SP-427; Noordwijk: ESA), 723
Moneti, A., Stolovy, S., Blommaert, J. A. D. L., Figer, D. F., & Najarro, F. 2001, A&A, 366, 106
Morris, M., & Serabyn, E. 1996, ARA&A, 34, 645
Morris, P. W., Stolovy, S., Wachter, S., Noriega-Crespo, A., Pannuti, T. G., & Hoard, D. W. 2006, ApJ, 640, L179
Odenwald, S. F., & Fazio, G. G. 1984, ApJ, 283, 601
Oka, T., Geballe, T. R., Goto, M., Usuda, T., & McCall, B. J. 2005, ApJ, 632, 882
Pahre, M. A., Ashby, M. L. N., Fazio, G. G., & Willner, S. P. 2004, ApJS, 154, 229
Pauls, T., & Mezger, P. G. 1975, A&A, 44, 259
Paumard, T., et al. 2006, ApJ, 643, 1011
Povich, M. S., et al. 2007, ApJ, 660, 346
Price, S. D., Egan, M. P., Carey, S. J., Mizuno, D. R., & Kuchar, T. A. 2001, AJ, 121, 2819
Ramírez, S., et al. 2008, ApJS, 175, 147
Reach, W. T., et al. 2005, PASP, 117, 978
———. 2006, AJ, 131, 1479
Rho, J., Reach, W. T., Lefloch, B., & Fazio, G. G. 2006, ApJ, 643, 965
Rodríguez-Fernández, N. J., & Martín-Pintado, J. 2005, A&A, 429, 923
Rodríguez-Fernández, N. J., Martín-Pintado, J., & de Vicente, P. 2001, A&A, 377, 631
Rodríguez-Fernández, N. J., Martín-Pintado, J., Fuente, A., & Wilson, T. L. 2004, A&A, 427, 217
Sahai, R., & Trauger, J. T. 1998, AJ, 116, 1357
Simpson, J. P., Colgan, S. W. J., Cotera, A. S., Erickson, E. F., Haas, M. R., Morris, M., & Rubin, R. H. 1997, ApJ, 487, 689
Simpson, J. P., Colgan, S. W. J., Cotera, A. S., Erickson, E. F., Hollenbach, D. J., Kaufman, M. J., & Rubin, R. H. 2007, ApJ, 670, 1115
Smith, H. A., Hora, J. L., Marengo, M., & Pipher, J. L. 2006, ApJ, 645, 1264
Spitzer, L. 1978, Physical Processes in the Interstellar Medium (New York: Wiley-Interscience)
Stark, A. A., Bally, J., Wilson, R. W., & Pound, M. W. 1989, in IAU Symp. 136, The Center of the Galaxy, ed. M. Morris (Dordrecht: Kluwer), 129
Stolovy, S., et al. 2006, J. Phys. Conf. Ser., 54, 176
Uchida, K., Morris, M., & Serabyn, E. 1990, ApJ, 351, 443
Uchida, K. I., Morris, M. R., Serabyn, E., & Bally, J. 1994, ApJ, 421, 505
Werner, M. W., et al. 2004, ApJS, 154, 1
Wilson, T. L., Ruf, K., Walmsley, C. M., Martin, R. N., Batrla, W., & Pauls, T. A. 1982, A&A, 115, 185
Yusef-Zadeh, F., Hewitt, J. W., & Cotton, W. 2004, ApJS, 155, 421
Yusef-Zadeh, F., Wardle, M., & Roy, S. 2007a, ApJ, 665, L123
Yusef-Zadeh, F., et al. 2007b, in IAU Symp. 242, Astrophysical Masers and Their Environments, ed. J. M. Chapman & W. A. Baan (Cambridge: Cambridge Univ. Press), 366
Zubko, V., Dwek, E., & Arendt, R. G. 2004, ApJS, 152, 211